

# Comparison of single breath hyperpolarized $^{129}\text{Xe}$ MRI with dynamic $^{19}\text{F}$ MRI in cystic fibrosis lung disease

Andrew McCallister<sup>1,2</sup> | Sang Hun Chung<sup>3</sup>  | Michael Antonacci<sup>1,2</sup>  | Margret Z. Powell<sup>4</sup> |  
Agathe S. Ceppe<sup>4</sup> | Scott H. Donaldson<sup>4,5</sup> | Yueh Z. Lee<sup>1,2,3,4,6</sup>  |  
Rosa Tamara Branca<sup>1,2</sup> | Jennifer L. Goralski<sup>4,5,7</sup>

<sup>1</sup>Department of Physics and Astronomy, The University of North Carolina, Chapel Hill, NC, USA

<sup>2</sup>Biomedical Research Imaging Center, The University of North Carolina, Chapel Hill, NC, USA

<sup>3</sup>Department of Biomedical Engineering, The University of North Carolina, Chapel Hill, NC, USA

<sup>4</sup>Marsico Lung Institute/UNC Cystic Fibrosis Center, The University of North Carolina, Chapel Hill, NC, USA

<sup>5</sup>Division of Pulmonary and Critical Care Medicine, The University of North Carolina, Chapel Hill, NC, USA

<sup>6</sup>Department of Radiology, The University of North Carolina, Chapel Hill, NC, USA

<sup>7</sup>Division of Pediatric Pulmonology, The University of North Carolina, Chapel Hill, NC, USA

## Correspondence

Jennifer Goralski, Marsico Lung Institute/  
UNC CF Research Center, The University  
of North Carolina, Campus Box 7248,  
125 Mason Farm Rd, Chapel Hill,  
NC 27599, USA.

Email: Jennifer\_goralski@med.unc.edu

## Funding information

National Institute of Diabetes and Digestive  
and Kidney Diseases,

Grant/Award Number: P30 DK065988

and DK108231; National Center for  
Advancing Translational Sciences, Grant/  
Award Number: UL1TR002489; Cystic

Fibrosis Foundation, Grant/Award Number:  
DONALD14XX0 and GORALS19Y5;

Doris Duke Charitable Foundation,

Grant/Award Number: 2015213

**Purpose:** To quantitatively compare dynamic  $^{19}\text{F}$  and single breath hyperpolarized  $^{129}\text{Xe}$  MRI for the detection of ventilation abnormalities in subjects with mild cystic fibrosis (CF) lung disease.

**Methods:** Ten participants with stable CF and a baseline FEV1 > 70% completed a single imaging session where dynamic  $^{19}\text{F}$  and single breath  $^{129}\text{Xe}$  lung ventilation images were acquired on a 3T MRI scanner. Ventilation defect percentages (VDP) values between  $^{19}\text{F}$  early-breath,  $^{19}\text{F}$  maximum-ventilation,  $^{129}\text{Xe}$  low-resolution, and  $^{129}\text{Xe}$  high-resolution images were compared. Dynamic  $^{19}\text{F}$  images were used to determine gas wash-in/out rates in regions of ventilation congruency and mismatch between  $^{129}\text{Xe}$  and  $^{19}\text{F}$ .

**Results:** VDP values from high-resolution  $^{129}\text{Xe}$  images were greater than from low-resolution images ( $P = .001$ ), although these values were significantly correlated ( $r = 0.68$ ,  $P = .03$ ). Early-breath  $^{19}\text{F}$  VDP and max-vent  $^{19}\text{F}$  VDP also showed significant correlation ( $r = 0.75$ ,  $P = .012$ ), with early-breath  $^{19}\text{F}$  VDP values being significantly greater ( $P < .001$ ). No correlation in VDP values were detected between either  $^{19}\text{F}$  method or high-res  $^{129}\text{Xe}$  images. In addition, the location and volume of ventilation defects were often different when comparing  $^{129}\text{Xe}$  and  $^{19}\text{F}$  images from the same subject. Areas of ventilation congruence displayed the expected ventilation kinetics, while areas of ventilation mismatch displayed abnormally slow gas wash-in and wash-out.

Andrew McCallister and Sang Hun Chung contributed equally to this manuscript.

This is an open access article under the terms of the Creative Commons Attribution-NonCommercial-NoDerivs License, which permits use and distribution in any medium, provided the original work is properly cited, the use is non-commercial and no modifications or adaptations are made.

© 2020 The Authors. *Magnetic Resonance in Medicine* published by Wiley Periodicals LLC on behalf of International Society for Magnetic Resonance in Medicine

**Conclusion:** In CF subjects, ventilation abnormalities are identified by both  $^{19}\text{F}$  and HP  $^{129}\text{Xe}$  imaging. However, these ventilation abnormalities are not entirely congruent.  $^{19}\text{F}$  and HP  $^{129}\text{Xe}$  imaging provide complementary information that enable differentiation of normally ventilated, slowly ventilated, and non-ventilated regions in the lungs.

**KEYWORDS**

cystic fibrosis, hyperpolarized gas, perfluorinated gas imaging, VDP, ventilation defect

## 1 | INTRODUCTION

Cystic fibrosis (CF) is the most common fatal monogenic disorder in Caucasians. The pathophysiology of CF includes the production of abnormally viscous mucus that obstructs airways and results in persistent infections and inflammation.<sup>1</sup> High-resolution computed tomography (HRCT) is currently the gold standard for assessing structural lung disease in CF; however, the risks associated with repeated radiation exposure limit the use of longitudinal HRCT, particularly in the pediatric population.<sup>2</sup> MRI is an emerging modality for analyzing lung structure and function as it is non-invasive with no ionizing radiation exposure and therefore, well-suited for longitudinal studies. Historically, structural lung MRI was limited due to short proton-signal transverse coherence time and low tissue density, but advances in ultrashort echo time (UTE) and zero echo time (ZTE) pulse sequences have allowed for improved structural imaging of lung parenchyma, blood vessels, and mucus plugging.<sup>3</sup> In addition to structural information, MRI has the potential to offer functional information in the form of ventilation imaging.<sup>4</sup>

Hyperpolarized (HP) gas imaging of the lungs has been performed for the better part of the past two decades with hyperpolarized helium-3 ( $^3\text{He}$ ). More recently, hyperpolarized xenon-129 ( $^{129}\text{Xe}$ ) has emerged as a more cost-effective and accessible alternative.<sup>4</sup> MRI images obtained with hyperpolarized  $^{129}\text{Xe}$  gas provide regional information about ventilation that standard pulmonary function tests alone cannot provide,<sup>5</sup> including a range of functional biomarkers, such as the ventilation defect percentage (VDP),<sup>6</sup> apparent diffusion coefficient (ADC),<sup>7</sup> and fractional ventilation.<sup>8</sup> VDP from  $^{129}\text{Xe}$  MR imaging correlates with lung clearance index (LCI) in pediatric subjects with CF,<sup>6</sup> and can possibly provide more specific and accurate information on CF treatment response in interventional trials.<sup>9</sup> In addition, due to the sizable tissue solubility and large chemical shift range ( $\sim 200$  ppm) of  $^{129}\text{Xe}$ , dissolved-phase HP  $^{129}\text{Xe}$  imaging is also feasible,<sup>10-12</sup> and could potentially provide valuable insights into the pulmonary gas-exchange processes in both healthy and CF lungs. Limiting

factors for HP  $^{129}\text{Xe}$  use are the need for technical expertise and special equipment to hyperpolarize the gas, as well as the known anesthetic effect of xenon.<sup>13</sup> However, recent studies have clearly shown that xenon inhalation for lung ventilation imaging is safe and well tolerated in adults as well as in children as young as 6 years old.<sup>14,15</sup>

Fluorine-19 ( $^{19}\text{F}$ ) imaging has been proposed as an alternative to HP gas for ventilation-space imaging that does not require on-site gas polarization. Feasibility studies have produced promising ventilation images using perfluoropropane ( $\text{C}_3\text{F}_8$  or PFP) combined with 21% oxygen ( $\text{O}_2$ ).<sup>16</sup> PFP has a high gyromagnetic ratio ( $\sim 3.4$  times  $^{129}\text{Xe}$ ), high natural abundance (100%), higher spin-density than  $^{129}\text{Xe}$ , and very short  $T_1$  (12.4 ms compared with  $\sim 20$  s for  $^{129}\text{Xe}$ ).<sup>16,17</sup> The short  $T_1$  allows for the use of very short repetition times (TRs) and signal averaging that increases the  $^{19}\text{F}$  image signal-to-noise ratio (SNR) without the need for pre-polarization. Without the need for a complex hyperpolarization protocol,  $^{19}\text{F}$  gas imaging could potentially provide an alternative means of characterizing regional lung ventilation.<sup>18</sup> Additionally, the absence of signal decay in the lung allows for multiple breath studies without the need of constant fresh supply of hyperpolarized gas, and the combination of low  $T_1$  and high spin density of  $^{19}\text{F}$  enables the quantification of gas wash-in and wash-out kinetics, thus, providing the ability to detect and localize ventilation abnormalities.<sup>19</sup> Ventilation defects have been observed in diseased populations using  $^{19}\text{F}$  imaging<sup>20</sup> and promising comparisons between  $^{19}\text{F}$  and  $^{129}\text{Xe}$  ventilation images have been recently performed in healthy volunteers.<sup>21</sup> As single breath-hold  $^{19}\text{F}$  imaging suffers from reduced SNR, preventing a true single breath-hold comparison between the two gases, here we compare dynamic  $^{19}\text{F}$  to single breath HP  $^{129}\text{Xe}$  MRI for the detection of lung ventilation defects in subjects with mild CF to better understand the similarities and differences between these two imaging approaches.

Due to the difference in resolutions between  $^{129}\text{Xe}$  and  $^{19}\text{F}$  images, we also compared low and high-resolution  $^{129}\text{Xe}$  images to isolate the potential effects of image resolution on the measurement of ventilation defects.

## 2 | METHODS

### 2.1 | Study participants and study design

This study was approved by the research ethics board at UNC-Chapel Hill (IRB 17-2569) and all participants provided written informed consent. Ten participants with stable CF lung disease,  $\geq 18$  y of age, non-smokers ( $<10$  pack-year history and no active smoking in the past year), and a baseline FEV<sub>1</sub>  $> 70\%$  predicted were enrolled from May 2018 to March 2019. Subject demographics are reported in Table 1. Subjects ranged in age from 21 to 44 years, and had a mean FEV<sub>1</sub> of  $81.7 \pm 15.0\%$  predicted. Each subject completed a single imaging session during which both <sup>19</sup>F and <sup>129</sup>Xe ventilation images were acquired in a random order. Prior to the imaging session, all subjects completed spirometry according to American Thoracic Society standards.<sup>22</sup>

### 2.2 | Imaging session

Imaging was performed on a Siemens PRISMA 3T MR scanner (Siemens AG) with multinuclear capabilities. Subjects were randomized to the order of <sup>19</sup>F and <sup>129</sup>Xe imaging; after the first scan, subjects exited the scanner and were allowed a 15-minute break, during which a single spirometric maneuver was completed to ensure no change in lung function as a result of either gas inhalation.

3D <sup>1</sup>H scans were completed before each <sup>129</sup>Xe and <sup>19</sup>F scan to facilitate co-registration of <sup>129</sup>Xe images with <sup>19</sup>F images. <sup>1</sup>H images acquired before <sup>129</sup>Xe scan were acquired during a breath hold of 1 L of medical air to improve matching of the lung volume at which <sup>1</sup>H and <sup>129</sup>Xe images were obtained and thus, image registration. All <sup>1</sup>H images were acquired by using a 3D stack of spiral VIBE sequence with 5° excitation flip angle, a TR of 2.42 ms, echo time (TE) of

0.05 ms, 224 by 224 acquisition matrix, and a resolution of 2.1 mm  $\times$  2.1 mm  $\times$  2.5 mm.

For <sup>19</sup>F acquisitions, a PFP-filled dual-cylinder lung phantom was scanned prior to each participant for quality assurance and to establish the <sup>19</sup>F center frequency. Subjects were positioned supine in the scanner with a <sup>19</sup>F-tuned 8-channel chest coil (ScanMed LLC, NE) around the chest. Subjects inhaled a pre-mixed, medical grade gas mixture of 79% PFP:21% oxygen (IND 122,215) using a continuous-breathing custom gas delivery device.<sup>20</sup> PFP was administered with a full-face non-invasive ventilation mask and a non-rebreathing Douglas Bag system. Subjects inhaled and exhaled one tidal volume breath of the contrast gas followed by a maximal inhalation with a 12 second breath-hold, during which time images were obtained prior to exhalation. A total of five such imaging cycles during PFP inhalation (wash-in) were performed, followed by up to eight cycles of room air inhalation (wash-out) until no visible signal was present (for a total for 10 wash-in breaths and up to 16 wash-out breaths). Ventilation was coached with a pneumotachometer as a visual aid for the MRI technician, and safety was monitored via blood oxygenation saturation, exhaled CO<sub>2</sub> concentration, and heart rate. <sup>19</sup>F dynamic images were acquired using a coronal 2D gradient echo (GRE) sequence with a 74° flip angle, an TE of 1.61 ms, a TR of 13 ms, 15 mm slice thickness, and a 64 by 64 acquisition matrix with a 130 Hz/pixel bandwidth and an in-plane resolution of 6.25 mm  $\times$  6.25 mm.

<sup>129</sup>Xe imaging was performed using a flexible <sup>129</sup>Xe-tuned quadrature chest coil (Clinical MR Solutions, WI). For each subject, two images were acquired, each during a single 12 second breath-hold of 750 ml isotopically enriched <sup>129</sup>Xe, polarized up to  $\sim 14\%$  with a Polarean 9800 <sup>129</sup>Xe Polarizer (Polarean, Inc, Durham, NC), mixed with 250 ml of N<sub>2</sub>. During the first inhalation, the <sup>129</sup>Xe center frequency was determined right before the acquisition of a low-resolution 2D multislice image data set. A high-resolution 2D multislice image data set was acquired during the second inhalation, approximately 30 minutes after the first inhalation using a second dose of hyperpolarized gas. Throughout the imaging session the subject's heart rate, blood pressure and oxygen saturation level were monitored every 5 min. After each xenon inhalation, subjects were also queried about symptoms associated with neurologic changes (ie, euphoria, numbness, tingling, etc). <sup>129</sup>Xe images were acquired using 2D GRE multislice sequences with a 10° excitation flip angle, a TR of 9 ms, an TE of 4 ms, a field of view of 280  $\times$  350 (read  $\times$  phase), and a matrix size of either 128  $\times$  64 with a slice thickness of 21.0 mm, which resulted in an in-plane resolution of 2.2 mm  $\times$  6.4 mm (low resolution) with a total scan time of 7 s, or a matrix size of 128  $\times$  80 with a slice thickness of 10.5 mm, which resulted in an in-plane resolution of 2.2 mm  $\times$  4.4 mm (high resolution) and a total scan time of 14 s.

**TABLE 1** Study population demographics

Gender	Age	FEV1 (%)	Genotype
F	20	73	F508del/F508del
F	27	72	W1282X/S341P
F	23	82	F508del/F508del
M	26	86	F508del/G551D
F	24	92	F508del/F508del
M	24	71	F508del/621 + 1G-->T
F	44	64*	R75X/R1066H
M	24	85	F508del/F508del
M	35	75	F508del/F508del
F	30	117	F508del/F508del

\*Visit FEV<sub>1</sub> below baseline due to subject not performing their normal airway clearance procedure on the day of the study visit.

## 2.3 | Image analysis

Registration and masking of images were performed using MIM Software (Cleveland, OH). The  $^1\text{H}$  lung masks corresponding to the  $^{129}\text{Xe}$  acquisitions were generated via a semi-automated segmentation of the  $^1\text{H}$  lung-cavity images, using a simple region-growing algorithm. The  $^1\text{H}$  lung masks corresponding to the  $^{19}\text{F}$  acquisitions were generated through visual inspection using the threshold and manual region of interest (ROI) segmentation tools due to difference in lung inflation between the  $^1\text{H}$  and  $^{19}\text{F}$  in some subjects. The  $^1\text{H}$  lung cavity images were used as lung masks to eliminate noise regions outside the lung ROI. Two sets of  $^{19}\text{F}$  ventilation type images were created for each subject; an early-breath image and a maximum ventilation (max-vent) breath image. For the early-breath image, the first image to show  $^{19}\text{F}$  signal was used<sup>21</sup>; for the max-vent image, the last wash-in image was used.  $^{129}\text{Xe}$  low-resolution (low-res) and high-resolution (high-res) were obtained as noted above.  $^{129}\text{Xe}$  and  $^{19}\text{F}$  images were then registered through a rigid registration transform on their respective  $^1\text{H}$  images. The registered images and masks were then exported to MATLAB (version 2017b; MathWorks, Natick, MA) for further processing using in-house scripts.

The algorithmic VDP segmentations commonly used in  $^{129}\text{Xe}$  studies, such as k-means clustering, are SNR dependent, and therefore, it is difficult to use these segmentations to make comparisons across modalities with different SNRs.<sup>23</sup> In this study, the SNR was calculated as the ratio of the 90th percentile of the lung interior distribution to the noise signal SD (taken from an ROI outside the thorax). As expected,  $^{19}\text{F}$  images had markedly lower SNR than  $^{129}\text{Xe}$  images, and this difference between SNR values drove the decision to use a threshold-based VDP analysis for all image types.<sup>17,18</sup> The intensity threshold was subsequently defined as the 95th percentile of the background noise distribution,<sup>18</sup> measured from an ROI drawn outside of the thorax. VDP was then defined as the percentage of the total lung volume that failed to exceed this intensity threshold.<sup>18</sup>

Analysis next focused on regions where localization of ventilation defects by  $^{129}\text{Xe}$  and  $^{19}\text{F}$  yielded disparate results. For this analysis, max-vent  $^{19}\text{F}$  image was fused with the  $^{129}\text{Xe}$  image using MIM software using a rigid body translation with no size dilations. The use of a rigid transformation versus a non-affine transformation was dictated by the absence of a theoretical model of lung inflation that is needed to accurately perform a non-affine transformation on the images. It is also important to note that, in the case of CF, the elastic properties of the lung tissue may be significantly altered by the presence of chronic inflammation. Such theoretical models are, therefore, expected to be subject specific, thus, introducing new confounding variables in the analysis.

After the rigid transformation, ROIs were manually drawn to identify regions where ventilation defects identified by the two techniques were mismatched. These regions

included locations where  $^{129}\text{Xe}$  was present but  $^{19}\text{F}$  was low/missing ( $^{129}\text{Xe} + ^{19}\text{F}-$ ) and locations where  $^{129}\text{Xe}$  was low/missing but  $^{19}\text{F}$  was present ( $^{129}\text{Xe}- ^{19}\text{F}+$ ). A set of ROIs for each subject were also examined in regions where both  $^{129}\text{Xe}$  and  $^{19}\text{F}$  were present ( $^{129}\text{Xe} + ^{19}\text{F}+$ ) for comparison.

Since the  $^{19}\text{F}$  dynamic imaging allows calculation of regional wash-in and wash-out kinetics, we compared PFP gas wash-in and wash-out rate constants in both matched areas (filled with both  $^{19}\text{F}$  and  $^{129}\text{Xe}$ ) and unmatched areas ( $^{19}\text{F}$  only or  $^{129}\text{Xe}$  only). The mean  $^{19}\text{F}$  signal in each ROI at each image acquisition time point was evaluated to generate a signal versus time plot for each ROI. The average of ROI voxels from a pre-PFP exposure scan was used to estimate the baseline noise level. The mean  $^{19}\text{F}$  signal values were then curve-fitted as a non-linear bi-exponential function<sup>24</sup> using the non-linear least squares method. The time constants that describe gas wash-in ( $\tau_1(\text{s})$ ) and wash-out ( $\tau_2(\text{s})$ ) kinetics, and the maximum  $^{19}\text{F}$  signal (peak), were derived from this fit.

## 2.4 | Statistical analysis

Statistical analyses were performed using Matlab and SAS v9.4. Linear regressions and Pearson correlations were performed between VDP values measured by low and high-resolution  $^{129}\text{Xe}$  and  $^{19}\text{F}$  imaging. VDP mean differences are reported as [absolute] % difference and displayed in Bland-Altman plots. The goodness of fit between mean raw  $^{19}\text{F}$  values in ROIs and fitted curves were assessed with R-square values. Repeated measures analysis of variance (ANOVA) was used to compare SNR, mean  $\tau_1$  and  $\tau_2$  values in the  $^{129}\text{Xe} + ^{19}\text{F}+$ ,  $^{129}\text{Xe} + ^{19}\text{F}-$  and  $^{129}\text{Xe}- ^{19}\text{F} +$  ROIs, and the peak  $^{19}\text{F}$  signal in each ROI. Comparisons between all groups were corrected with the Tukey-Kramer adjustment. Results are reported as mean  $\pm$  SD and displayed in Table 2.  $P$ -values  $< 0.05$  were considered significant.

# 3 | RESULTS

## 3.1 | Signal to noise

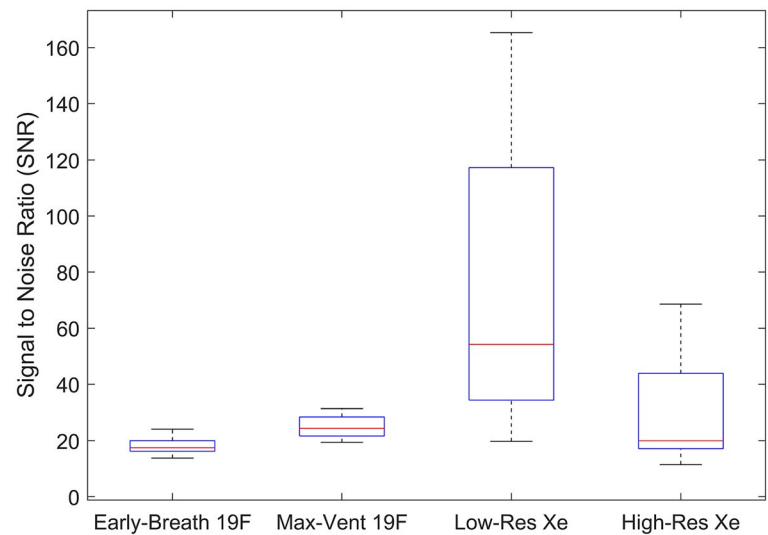
Signal to noise values across the entire lung volume were determined in the early-breath  $^{19}\text{F}$ , max-vent  $^{19}\text{F}$ , low-resolution  $^{129}\text{Xe}$ , and high-resolution  $^{129}\text{Xe}$  images as shown in Figure 1 (early-breath  $^{19}\text{F}$ :  $18.36 \pm 3.16$ ; max-vent  $^{19}\text{F}$ :  $25.02 \pm 4.02$ ; low-res  $^{129}\text{Xe}$ :  $73.59 \pm 53.82$ , high-res  $^{129}\text{Xe}$ :  $30.17 \pm 20.82$ ). Significant SNR differences were present between early-breath  $^{19}\text{F}$  images vs. low-res  $^{129}\text{Xe}$  images ( $P = .041$ ) and between early-breath  $^{19}\text{F}$  vs. max-vent  $^{19}\text{F}$  ( $P < .001$ ). A nearly significant difference between low-res  $^{129}\text{Xe}$  vs. High-res  $^{129}\text{Xe}$  was observed ( $P = .052$ ).

**TABLE 2** Results of repeated measures ANOVA on time constants  $\tau_1$ ,  $\tau_2$ , and peak signal. Comparison of  $^{129}\text{Xe} + ^{19}\text{F}+$  (ROI B) and  $^{129}\text{Xe}-^{19}\text{F}+$  (ROI C) showed significant difference for  $\tau_2$  ( $P = .0075$ )

	ROI type (mean $\pm$ SD)			Corrected $P$ values (Tukey Kramer) $P$ -values		
	Xe + F19- (ROI A)	Xe + F19+ (ROI B)	Xe- F19+ (ROI C)	Comparison A-B	Comparison B-C	Comparison A-C
Tau1 (s)	70.46 $\pm$ 38.70	36.83 $\pm$ 11.56	85.36 $\pm$ 56.83	0.3397	0.0589	0.7601
Tau2 (s)	31.16 $\pm$ 33.35	18.13 $\pm$ 5.52	34.31 $\pm$ 11.63	0.4947	0.0075	0.9294
Peak Signal Intensity	9.87 $\pm$ 14.55	53.59 $\pm$ 17.15	37.01 $\pm$ 8.36	<0.0001	0.0192	0.0002

Note: All comparisons of peak values were statistically significant, indicating that the  $^{19}\text{F}$  signal at the end of the dynamic imaging cycle was able to discriminate between the three different types of ROIs.

**FIGURE 1** Boxplot showing distribution of ventilation images SNRs across all ten subjects, with the median (red line), 25th and 75th percentiles (blue box edges), and range (whiskers) displayed. Statistically significant differences were seen in early-breath  $^{19}\text{F}$  vs. low-res  $^{129}\text{Xe}$  ( $P = .041$ ) and early-breath  $^{19}\text{F}$  vs. max-vent  $^{19}\text{F}$  ( $P < .001$ )



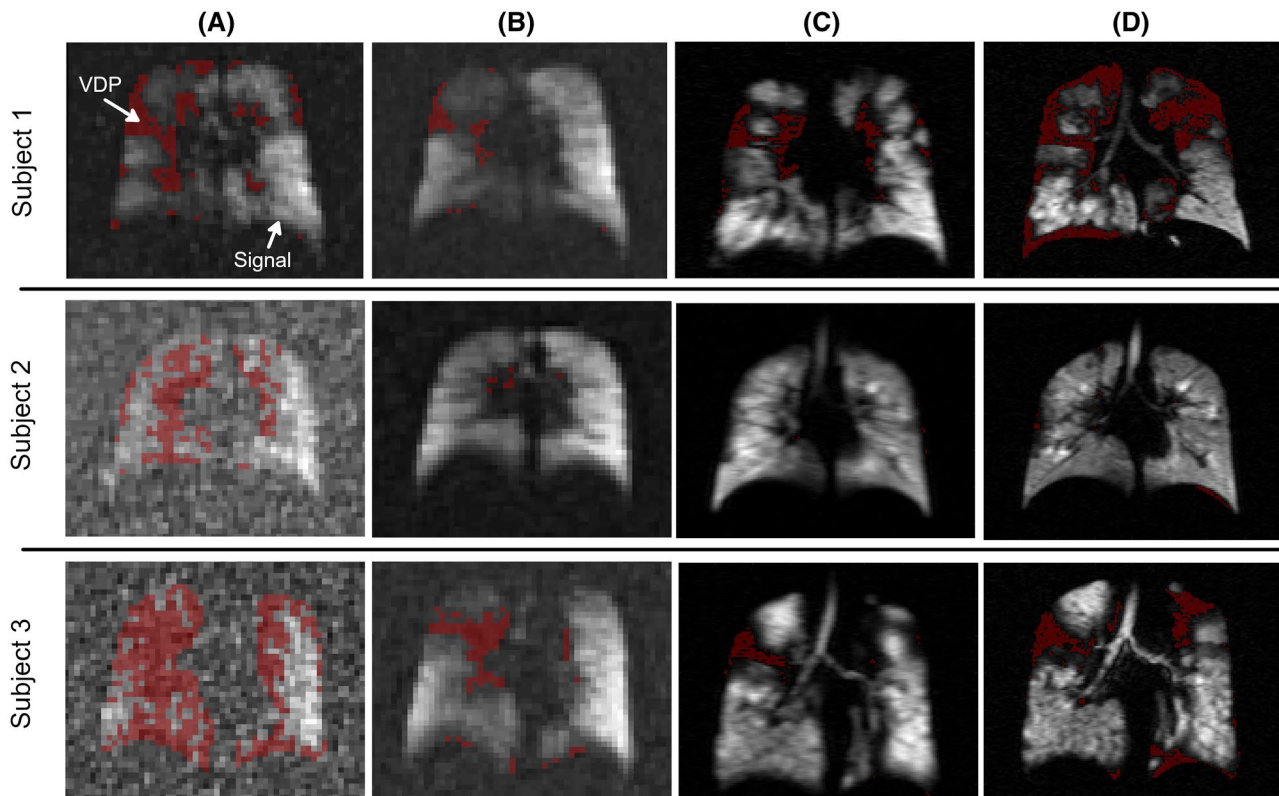
### 3.2 | Comparison of ventilation defect values across methods

Figure 2 provides examples of the variability of gas filling between methods. In Subject 1, the ventilation defect location and volume from the early-breath  $^{19}\text{F}$  was similar to that of the high-resolution  $^{129}\text{Xe}$ . In contrast, the max-vent  $^{19}\text{F}$  showed eventual filling of a majority of these ventilation defects. In Subject 2, while neither  $^{129}\text{Xe}$  images nor the max-vent  $^{19}\text{F}$  images demonstrated significant ventilation defects, the early-breath  $^{19}\text{F}$  images showed substantial defects that likely reflect inadequate SNR at this early time point. In Subject 3, the early-breath  $^{19}\text{F}$  image again shows large areas of ventilation defect in the right lung, thought to reflect inadequate gas uptake or signal at this early point of the PFP wash-in cycle. The high-resolution  $^{129}\text{Xe}$  image detected more ventilation defects than the low-resolution  $^{129}\text{Xe}$  image, especially in the left upper lobe, for example, where volume averaging may be increasing the local mean value above the threshold. Comparison of the max-vent  $^{19}\text{F}$  and xenon images shows both matched  $^{129}\text{Xe}-^{19}\text{F}$ - and mismatched  $^{129}\text{Xe}-^{19}\text{F}+$  ventilation defects, suggesting that some lung

regions never filled with PFP, whereas others demonstrated delayed filling.

Figure 3 shows correlations and Bland-Altman plots of VDPs calculated from each image type, referenced against the standard high-res  $^{129}\text{Xe}$  VDP method. No correlation between early-breath  $^{19}\text{F}$  VDP ( $r = 0.28$ ,  $P = .43$ ; Figure 3A) or max-vent  $^{19}\text{F}$  VDP ( $r = 0.23$ ,  $P = .52$ ; Figure 3B) and high-res  $^{129}\text{Xe}$  VDP values were observed. The Bland-Altman plot shows a significant mean difference in VDP between max-vent  $^{19}\text{F}$  and high-res  $^{129}\text{Xe}$  ( $-10.6\%$ ,  $P = .007$ ; Figure 3E). There was no significant difference in mean VDP values between early-breath  $^{19}\text{F}$  and high-res  $^{129}\text{Xe}$  ( $-0.5\%$ ,  $P = .87$ ; Figure 3D). In contrast, low-res vs. high-res  $^{129}\text{Xe}$  VDP display a significant correlation ( $r = 0.68$ ,  $P = .03$ ; Figure 3C), although a significant mean difference in VDP ( $-10.5\%$ ,  $P = .001$ ; Figure 3F) indicated consistent underestimation of VDP values by low-res  $^{129}\text{Xe}$  images.

Figure 4 shows the comparison between max-vent  $^{19}\text{F}$  VDP and early-breath  $^{19}\text{F}$  VDP. There was significant correlation ( $r = 0.75$ ,  $P = .012$ ) and a significant mean difference ( $10.0\%$ ,  $P = 4.9\text{e-}5$ ) indicating overestimation of VDP by early breath  $^{19}\text{F}$ .



**FIGURE 2** Representative images showing early-breath  $^{19}\text{F}$  (A), max-vent  $^{19}\text{F}$  (B), low-resolution  $^{129}\text{Xe}$  (C), and high-resolution  $^{129}\text{Xe}$  (D) images in three subjects. A threshold was applied to define regions of ventilation defects (red masks). VDPs were calculated as the percentage of lung with a ventilation defect compared with total lung volume calculated by the anatomic mask. VDPs in early-breath  $^{19}\text{F}$  images were higher than in max-vent images, likely due to lack of sufficient signal. High-resolution  $^{129}\text{Xe}$  images typically displayed higher VDPs than low-res images

### 3.3 | Evaluating mismatched $^{19}\text{F}$ and $^{129}\text{Xe}$ ventilation defects

Comparison of low-resolution and high-resolution  $^{129}\text{Xe}$  images did not reveal any region of non-congruency that could not be attributed to differences in resolution: high-resolution ventilation images consistently displayed sharper ventilation defects than the low-resolution images. In contrast, within the same subject, we observed differences in the location and volume of ventilation defects when comparing  $^{129}\text{Xe}$  and  $^{19}\text{F}$  images (Figure 5). We sought to utilize the dynamic ventilation data afforded by  $^{19}\text{F}$  imaging to further understand the nature of these mismatched regions. In Figure 6, representative mean  $^{19}\text{F}$  signal vs. time curves in matched and unmatched ROIs are shown. Mean  $^{19}\text{F}$  wash-in ( $\tau_1$ ) and wash-out ( $\tau_2$ ) rate constants derived from these plots, along with the goodness of fit (r-square), from each ROI type ( $^{129}\text{Xe} + ^{19}\text{F}+$ ,  $^{129}\text{Xe} + ^{19}\text{F}-$ , and  $^{129}\text{Xe}-^{19}\text{F}+$ ) are shown with box plots in Figure 7. Wash-in and wash-out rate constants ( $\tau_1$  and  $\tau_2$ , respectively) were higher in both types of mismatched ROIs ( $^{129}\text{Xe}-^{19}\text{F}+$  and  $^{129}\text{Xe} + ^{19}\text{F}-$ ) when compared with matched ROI ( $^{129}\text{Xe} + ^{19}\text{F}+$ ) regions, but only  $^{129}\text{Xe} + ^{19}\text{F}+$  vs.  $^{129}\text{Xe}-^{19}\text{F}+$  +  $\tau_2$  showed significant difference ( $P = .008$ ). The mean maximum  $^{19}\text{F}$  signal value derived from the modeled signal versus time plot was found to be statistically different

between all three different regions ( $^{129}\text{Xe}-^{19}\text{F}+$ ,  $^{129}\text{Xe} + ^{19}\text{F}-$ , and  $^{129}\text{Xe} + ^{19}\text{F}+$ ), as shown in Table 2. This demonstrates that lung regions with  $^{19}\text{F}$ , but no  $^{129}\text{Xe}$ , do indeed fill, but at a slower rate and to a lower peak signal (compared with defect-free ROIs). More surprising is the paradoxical finding of lung regions with  $^{129}\text{Xe}$  signal after a single breath, but very low  $^{19}\text{F}$  signal after multiple breaths. Examination of  $^{19}\text{F}$  wash-in/out time constants and peak signals in these regions suggests that they also have abnormal ventilation kinetics, yet are not detected as abnormal by the  $^{129}\text{Xe}$  method. Because poorly estimated  $\tau_1$  and  $\tau_2$  values could lead to misinterpretation of our data, we calculated the goodness of fit for  $^{19}\text{F}$  signal in each type of ROI to assess the quality of the data. Importantly, the r-square values between raw data and calculated exponential curves were very high in each type of ROI, including those with low  $^{19}\text{F}$  signal, providing confidence in these observations ( $R^2 = 0.89 \pm 0.18$  for  $^{129}\text{Xe} + ^{19}\text{F}-$ ,  $0.99 \pm 0.003$  for  $^{129}\text{Xe} + ^{19}\text{F}+$ , and  $0.99 \pm 0.01$  for  $^{129}\text{Xe}-^{19}\text{F}+$ ).

## 4 | DISCUSSION

This study reports a first comparison of regional lung ventilation as assessed by dynamic  $^{19}\text{F}$  and HP  $^{129}\text{Xe}$  MRI imaging in CF subjects. The sequential performance of  $^{19}\text{F}$  and

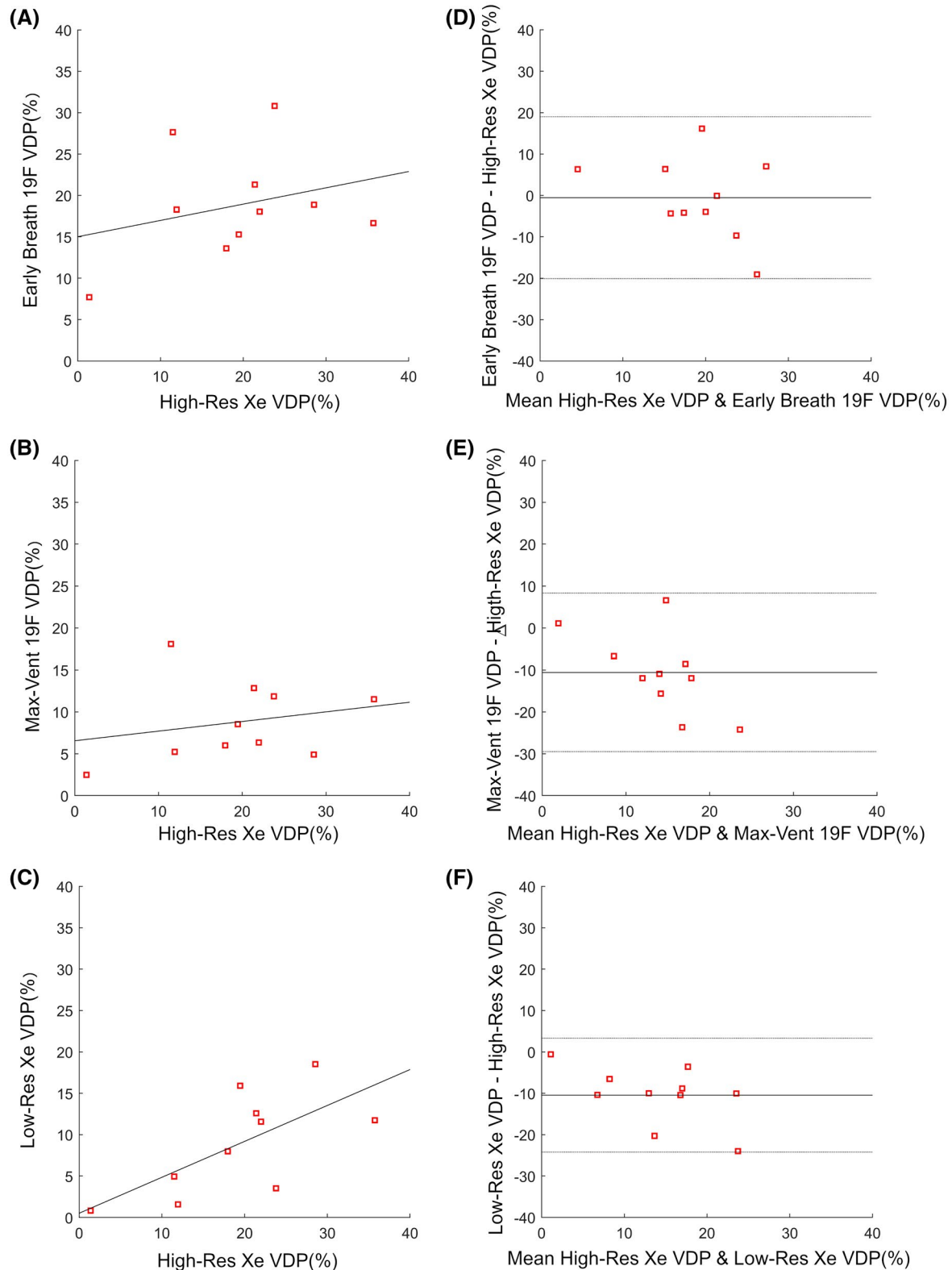


**FIGURE 3** Scatter (A, B, C) and Bland-Altman (D, E, F) plots comparing VDP measurements. Regression line (dark gray) shown on scatter plots. Mean bias  $\pm$  95% lines of agreement shown on Bland-Altman plots. High-resolution  $^{129}\text{Xe}$  is compared with: early-breath  $^{19}\text{F}$  images ( $r = 0.28$ ,  $P = .43$ . Estimated bias =  $-0.5 \pm 19.6\%$ ,  $P = .87$ ) (A,D); (B, E). max-vent  $^{19}\text{F}$  images ( $r = 0.23$ ,  $P = .52$ . Estimated bias =  $-10.6 \pm 18.9\%$ ,  $P = .007$ ) (B,E); low-resolution  $^{129}\text{Xe}$  ( $r = 0.68$ ,  $P = .03$  (C,F). Estimated bias =  $-10.5\% \pm 13.8\%$ ,  $P = .001$ )

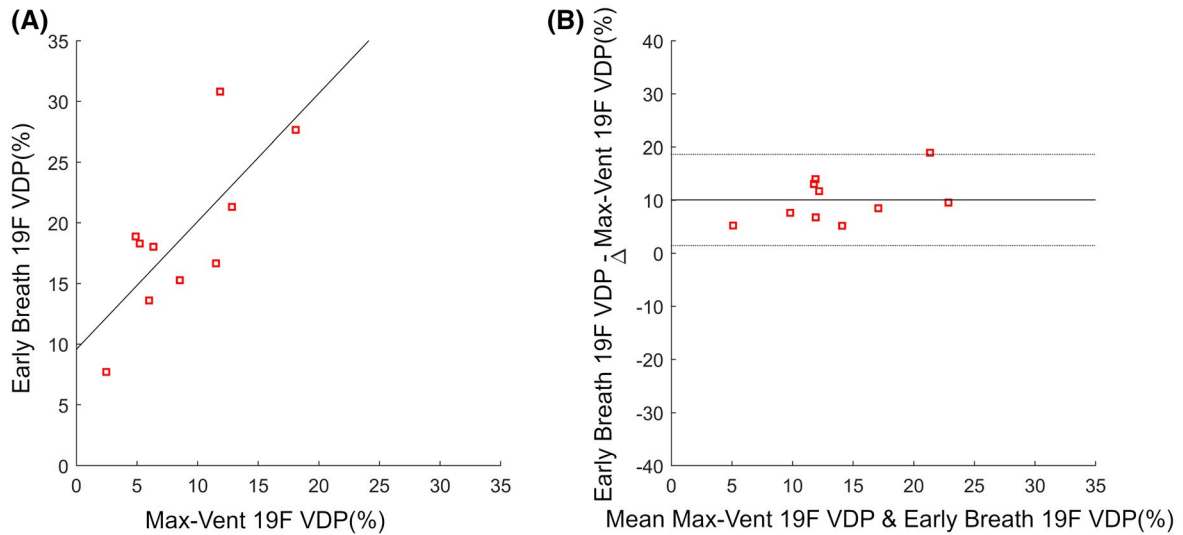


**FIGURE 4** Scatter plot (A) and Bland-Altman plot (B) showing the comparison of VDP measurements from max-vent <sup>19</sup>F VDP and early-breath <sup>19</sup>F VDP. The correlation was  $r = 0.75$ ,  $P = .01$ . The Bland-Altman plot shows estimated bias =  $10.05 \pm 8.6\%$  with  $P = 4.9e-5$

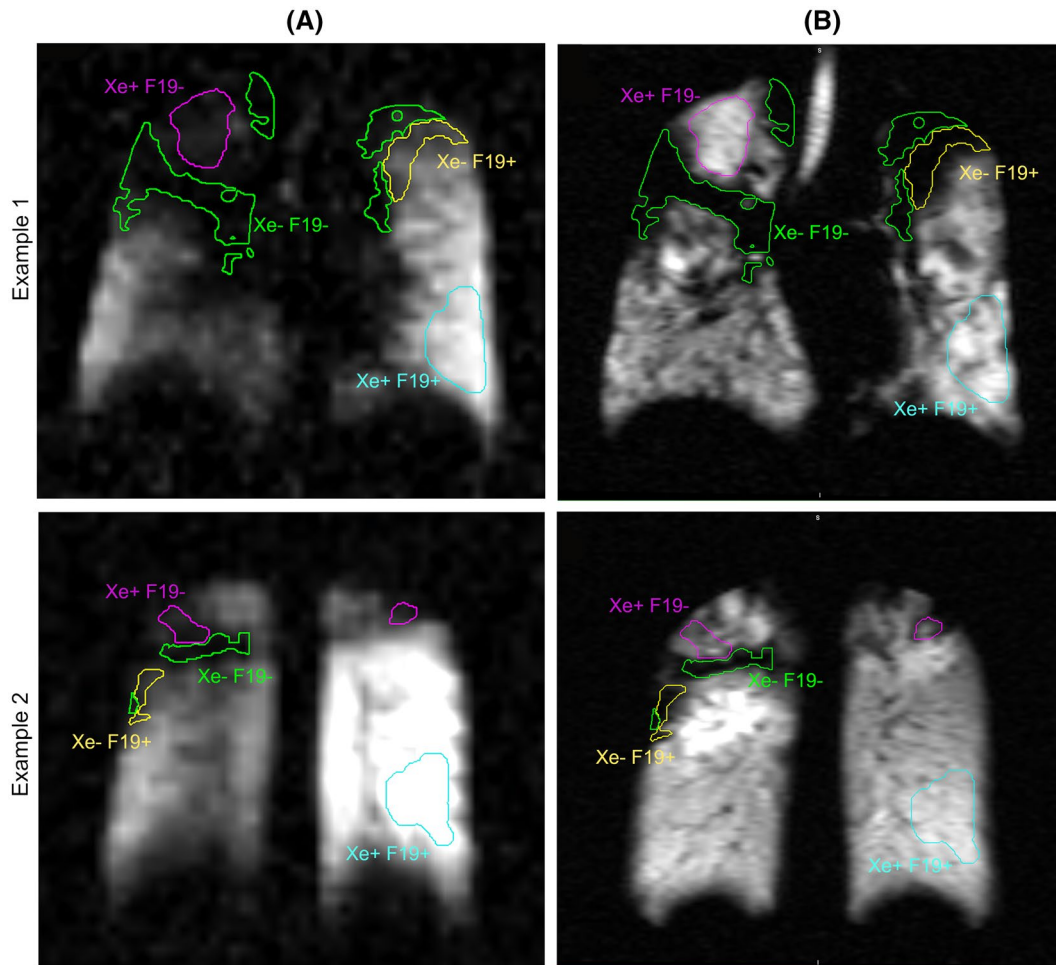


**FIGURE 5** Examples of mismatched ventilation signal from two subjects. A. max-vent <sup>19</sup>F and B. high-resolution <sup>123</sup>Xe images. The purple ROI outlines <sup>129</sup>Xe + <sup>19</sup>F- regions; the yellow ROI outlines <sup>129</sup>Xe-<sup>19</sup>F+ regions; the cyan ROI outlines a matched <sup>129</sup>Xe + <sup>19</sup>F+ region used for comparison. The green ROI outlines a matched <sup>129</sup>Xe-<sup>19</sup>F- for additional comparison



$^{129}\text{Xe}$  MRI scans within the same day in subjects with mild CF lung disease provided a powerful platform to make comparisons between these modalities.

As expected,  $^{19}\text{F}$  images were characterized by a markedly lower SNR, which prevented direct comparison of single breath  $^{129}\text{Xe}$  ventilation images to single breath  $^{19}\text{F}$  images. Therefore, we compared early-breath  $^{19}\text{F}$  images (ie, after first appearance of signal during the multiple breath wash-in procedure) to single breath  $^{129}\text{Xe}$  images. However, when assessed after multiple PFP breaths, SNR increased as expected, and a portion of ventilation defects disappeared, indicating

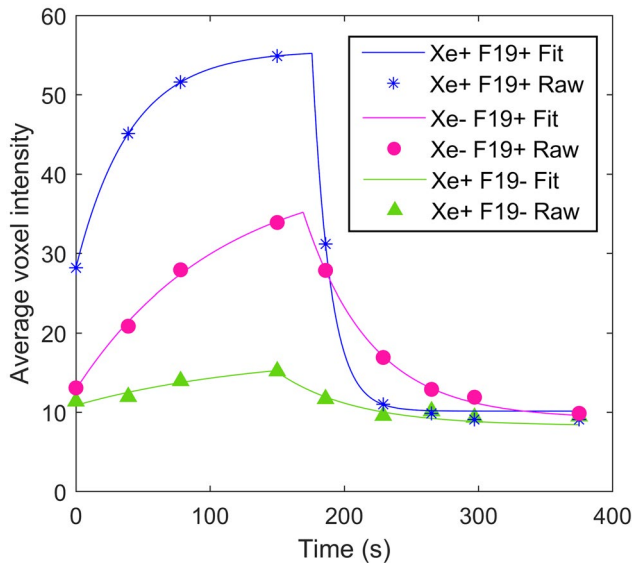


**FIGURE 6** Plots of the raw (symbols) and modeled (lines)  $^{19}\text{F}$  signal time course in matched ( $^{129}\text{Xe} + ^{19}\text{F}+$ ; blue) and unmatched ( $^{129}\text{Xe}-^{19}\text{F}+$  and  $^{129}\text{Xe} + ^{19}\text{F}-$ ; red and green, respectively) ROIs from a single representative subject. In all subjects with mismatched ROIs, a consistent rank order of maximum gas  $^{19}\text{F}$  signal of  $^{129}\text{Xe} + ^{19}\text{F}+ > ^{129}\text{Xe}-^{19}\text{F}+ > ^{129}\text{Xe} + ^{19}\text{F}-$  was observed despite accentuated  $^{129}\text{Xe}$  signal (ie, higher than mean lung signal) in some of the  $^{129}\text{Xe} + ^{19}\text{F}-$  ROIs.

that many ventilation defects detected by single breath  $^{129}\text{Xe}$  MRI ultimately do fill during the multiple breath wash-in cycle. What is unclear from this data, however, is whether the filling was due to direct versus collateral ventilation.

When measuring VDP values, image resolution also played a role. In our study, direct comparison of VDP values from high-resolution  $^{129}\text{Xe}$  and low-resolution  $^{129}\text{Xe}$  ventilation images allowed for the isolation of the effect of resolution on VDP. As expected, relative to high-res  $^{129}\text{Xe}$  scans, low-res  $^{129}\text{Xe}$  scans were more prone to partial volume effects and consistently underestimated VDP. This underestimation is larger at higher VDPs, with the trend showing low-res scans underestimate VDP by about 50%. It is important to note that the size of the VDP underestimation in the low-resolution  $^{129}\text{Xe}$  images is a function of the specific signal intensity threshold used. In particular, by using a less conservative signal threshold, some additional ventilation defects could be captured in the low-resolution  $^{129}\text{Xe}$  images, resulting into higher VDP values.

Our data also suggest that VDP may be overestimated by single breath approaches (early-breath  $^{19}\text{F}$ , low-res  $^{129}\text{Xe}$ , high-res  $^{129}\text{Xe}$ ), which consistently measured higher VDPs than those determined via max-vent  $^{19}\text{F}$  images. Since slow filling regions appear as regions of ventilation defects in single-breath hold images, they cannot be differentiated from regions of true ventilation defects. To this end, the multiple breath protocol employed for  $^{19}\text{F}$  imaging provides the ability to differentiate between true ventilation defects and slow filling regions, by providing wash-in and wash-out gas kinetics. In particular, in areas of congruence ( $^{129}\text{Xe} + ^{19}\text{F}+$  or  $^{129}\text{Xe}-^{19}\text{F}-$ ), ventilation kinetics were as expected, with either rapid or absent ventilation, respectively. In regions that were  $^{129}\text{Xe}-^{19}\text{F}+$ , on the contrary, the multiple breath PFP protocol was able to demonstrate that these regions were not truly unventilated, but, rather, slow to fill. Because HP  $^{129}\text{Xe}$  images are acquired using a single breath technique, these slowly filling regions could not be differentiated from true non-filling

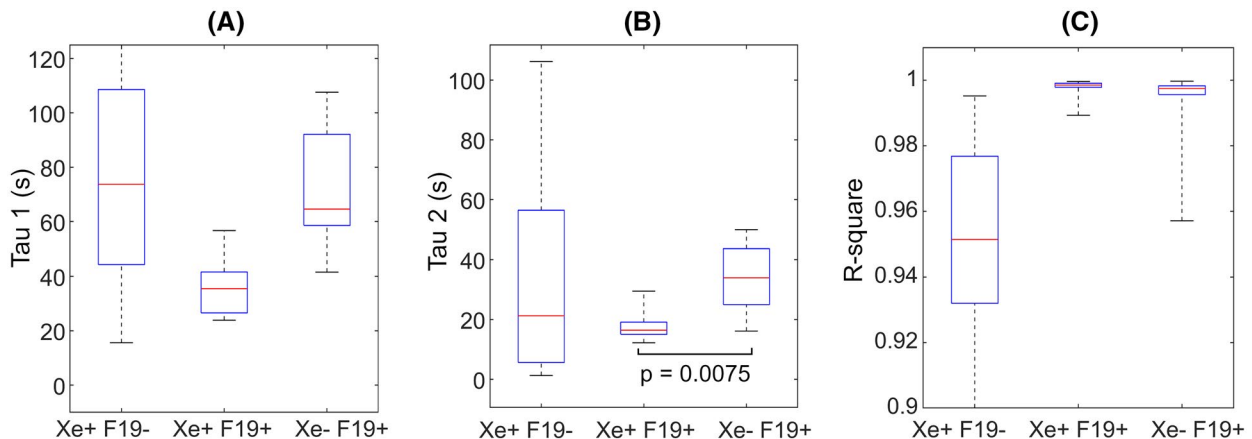


**FIGURE 7** Box plots of wash-in ( $\tau_1$ ) (A) and wash-out ( $\tau_2$ ) (B) time constants from the  $^{19}\text{F}$  bi-exponential fit. c. R-square indicates the goodness of the fit between raw data and modeled curves. The horizontal brackets indicate statistical significance with corresponding  $P$ -values

regions. As such, dynamic imaging using  $^{19}\text{F}$  provides additional capability to characterize these abnormal regions.

The observation of lung regions with a  $^{129}\text{Xe} + ^{19}\text{F}$ - pattern was unexpected, as multiple breaths of PFP is not expected to be less likely to fill a partially obstructed region than a single breath of  $^{129}\text{Xe}$ . The presence of  $^{129}\text{Xe}$  gas suggests that these areas must be receiving some ventilation, despite the paucity of  $^{19}\text{F}$  signal. The reduced  $^{19}\text{F}$  signal in these regions may be explained by the low SNR and diffusivity of the gas, when compared with  $^{129}\text{Xe}$ , coupled with an increase in airway resistance in the region, similarly to what has already been observed in  $^{129}\text{Xe}/^3\text{He}$  comparison studies in COPD patients.<sup>25</sup> The analysis of  $\tau_1$  and  $\tau_2$  rate constants, which we were able to characterize with a high degree of confidence despite the relatively low  $^{19}\text{F}$  signal, confirmed that in these lung regions, not only was peak  $^{19}\text{F}$  signal low, but also the rates of both gas wash-in and wash-out were markedly slowed. The presence of  $^{129}\text{Xe}$  signal (in some cases, even an accentuated  $^{129}\text{Xe}$  signal) in these regions could be explained by a reduced concentration of molecular oxygen in these poorly ventilated regions. This could theoretically be encountered in areas of gas trapping, where some contrast gas is able to enter the region, perhaps by collateral ventilation, but encounters an environment that is relatively devoid of oxygen. This would thereby reduce the rate of HP  $^{129}\text{Xe}$  depolarization and, in turn, cause a paradoxically higher  $^{129}\text{Xe}$  signal. If this is the case,  $^{129}\text{Xe}$  MRI may at times under-report true ventilation defects, as the result of the complex relationship between  $^{129}\text{Xe}$  polarization and the local lung oxygen tension. While further testing is required to fully assess gas trapping effects on  $^{129}\text{Xe}$  MRI images, our results show that the addition of dynamic  $^{19}\text{F}$  imaging in registration with HP  $^{129}\text{Xe}$  has provided important additional insights into lung ventilation dynamics.

The peak  $^{19}\text{F}$  value at the end of the inhalation sequences was also able to differentiate these three different filling patterns, suggesting that the delayed phase filling with PFP as a single parameter may be the most informative of the ventilation status (Table 2). Further work in other disease states could better inform the clinical utility of the dynamic  $^{19}\text{F}$  approaches. Although we did not perform repeatability scans as a part of this study, others have shown that dynamic  $^{19}\text{F}$  ventilation imaging, albeit with a different scanning protocol, has good repeatability in normal subjects and subjects with chronic obstructive pulmonary diseases.<sup>26</sup>

Several technical factors impacted our data, including challenges related to co-registration of  $^{19}\text{F}$ ,  $^{129}\text{Xe}$ , and  $^1\text{H}$  images. Proton images of the thoracic cavity and gas ventilation images were obtained during separate maximal inhalation breath-holds, making it likely that the same inspiratory capacity might not be reached consistently. As a result, differences in lung inflation volumes can be expected to cause co-registration errors, both in  $^{19}\text{F}$  and  $^1\text{H}$  images. This problem is avoided with the  $^{129}\text{Xe}$ -MRI method, as a fixed

inhalation volume can be achieved simply through the use of a fixed volume gas delivery bag. Differences in lung inflation may have led to additional ventilation defects around the lung edges. Thus, the ability to simultaneously acquire anatomical and ventilation images within a single breath-hold, as done for HP ventilation imaging, would likely benefit the  $^{19}\text{F}$  method.<sup>27,28</sup> Recent work to accelerate  $^{19}\text{F}$  ventilation imaging, which could allow for acquisition of  $^{19}\text{F}/^1\text{H}$  images in a single breath hold, would accomplish this goal.<sup>29,30</sup> A related minor limitation for the study was the need to reposition the patient between the two inhaled gas studies.

Finally, the use of a multi-channel  $^{19}\text{F}$  lung coil led to  $B_1$  inhomogeneities that were subject and coil position dependent and could not be corrected.  $B_1$  inhomogeneities made ventilation thresholds position dependent, preventing the application of typical linear binning techniques that delineate regions of high, medium and low intensity areas based on universal thresholds.<sup>31</sup> Moreover, retrospective bias-field estimation techniques, often used to reduce subject-dependent  $B_1$  effects in  $^{129}\text{Xe}$  studies,<sup>31</sup> created spurious gas-filled regions from noise level intensity in low SNR  $^{19}\text{F}$  images. This is not surprising as these techniques have been developed for high-SNR images and, in  $^{19}\text{F}$  images, where SNR is on the order of the bias-field correction, they artificially change image intensities by a factor of 2 or 3.<sup>31,32</sup>

## 5 | CONCLUSIONS

In CF subjects, ventilation abnormalities are identified by both  $^{19}\text{F}$  and HP  $^{129}\text{Xe}$  imaging but are not entirely congruent across all areas of ventilation. The use of both modalities in this study allowed us to identify an “imaging phenotype” that resulted from normally ventilated, slowly ventilated, and non-ventilated regions. Although further work is needed to evaluate these techniques in other patient populations, these data strongly suggest the complimentary nature of  $^{19}\text{F}$  and HP  $^{129}\text{Xe}$  imaging; however, VDPs obtained from each method should not be considered equivalent. These data also highlight the utility of ventilation kinetic analyses with  $^{19}\text{F}$  MRI and the inherent limitations of relying on a single breath VDP assessment for the characterization of airway function.

## ACKNOWLEDGMENTS


This work was supported by the Cystic Fibrosis Foundation (DONALD14XX0 and GORALS19Y5) and the NIDDK (P30 DK 065988 and DK 108231). We gratefully acknowledge the regulatory assistance of the North Carolina Translational and Clinical Sciences (NC TraCS) Institute, which is supported by the National Center for Advancing Translational Sciences (NCATS), National Institute of Health, through Grant Award Number UL1TR002489. Dr Goralski also acknowledges support from the Doris Duke Charitable Foundation (Grant 2015213).

## DATA AVAILABILITY STATEMENT

All data and processing algorithms have been uploaded to the UNC Libraries Carolina Digital Repository and is available online at [https://cdr.lib.unc.edu/concern/data\\_sets/m900p0761?locale=en](https://cdr.lib.unc.edu/concern/data_sets/m900p0761?locale=en).

## ORCID

Sang Hun Chung  <https://orcid.org/0000-0002-0605-9420>

Michael Antonacci  <https://orcid.org/0000-0001-9363-3234>

Yueh Z. Lee  <https://orcid.org/0000-0003-1846-7680>

## REFERENCES

- Collins FS. Cystic fibrosis: Molecular biology & therapeutic implications. *Science* (80- ). 1992;256:774-779.
- Eichinger M, Heussel CP, Kauczor HU, Tiddens H, Puderbach M. Computed tomography and magnetic resonance imaging in cystic fibrosis lung disease. *J Magn Reson Imaging*. 2010;32:1370-1378.
- Johnson KM, Fain SB, Schiebler ML, Nagle S. Optimized 3D ultrashort echo time pulmonary MRI. *Magn Reson Med*. 2013;70:1241-1250.
- Roos JE, McAdams HP, Kaushik SS, Driehuis B. Hyperpolarized gas MRI: Technique and applications. *Magn Reson Imaging Clin N Am*. 2016;23:217-229.
- Altes TA, Eichinger M, Puderbach M. Magnetic resonance imaging of the lung in cystic fibrosis. *Proc Am Thorac Soc*. 2007;4:321-327.
- Kanhere N, Couch MJ, Kowalik K, et al. Correlation of lung clearance index with hyperpolarized 129Xe magnetic resonance imaging in pediatric subjects with cystic fibrosis. *Am J Respir Crit Care Med*. 2017;196:1073-1075.
- Ouriadov A, Farag A, Kirby M, McCormack DG, Parraga G, Santyr GE. Lung morphometry using hyperpolarized 129Xe apparent diffusion coefficient anisotropy in chronic obstructive pulmonary disease. *Magn Reson Med*. 2013;70:1699-1706.
- Hamedani H, Clapp JT, Kadlecck SJ, et al. Regional fractional ventilation by using multibreath wash-in 3He MR imaging. *Radiology*. 2017;285:1063-1063.
- Thomen RP, Walkup LL, Roach DJ, Cleveland ZI, Clancy JP, Woods JC. Hyperpolarized 129Xe for investigation of mild cystic fibrosis lung disease in pediatric patients. *J Cyst Fibros*. 2017;16:275-282.
- Ebner L, Kammerman J, Driehuis B, Schiebler ML, Cadman RV, Fain SB. The role of hyperpolarized 129xenon in MR imaging of pulmonary function. *Eur J Radiol*. 2017;86:343-352.
- Zhang L, Burant A, McCallister A, et al. Accurate MR thermometry by hyperpolarized 129Xe. *Magn Reson Med*. 2016;78:1070-1079.
- Rao M, Stewart NJ, Norquay G, Griffiths PD, Wild JM. High resolution spectroscopy and chemical shift imaging of hyperpolarized 129Xe dissolved in the human brain in vivo at 1.5 Tesla. *Magn Reson Med*. 2016;75:2227-2234.
- Kennedy RR, Stokes JW, Downing P. Anaesthesia and the “inert” gases with special reference to xenon. *Anaesth Intensive Care*. 1992;20:66-70.
- Shukla Y, Wheatley A, Kirby M, et al. Hyperpolarized 129Xe magnetic resonance imaging. Tolerability in healthy volunteers and subjects with pulmonary disease. *Acad Radiol*. 2012;19:941-951.
- Walkup LL, Thomen RP, Akinyi TG, et al. Feasibility, tolerability and safety of pediatric hyperpolarized 129Xe magnetic resonance imaging in healthy volunteers and children with cystic fibrosis. *Pediatr Radiol*. 2016;46:1651-1662.
- Couch MJ, Ball IK, Li T, et al. Pulmonary ultrashort echo time 19F MR imaging with inhaled fluorinated gas mixtures in healthy volunteers: Feasibility. *Radiology*. 2013;269:903-909.
- Couch MJ, Ball IK, Li T, Fox MS, Biman B, Albert MS. 19F MRI of the lungs using inert fluorinated gases: Challenges and new developments. 2019;49:343-354.
- Gutberlet M, Kaireit TF, Voskrebenezv A, et al. Free-breathing dynamic (19F) gas MR imaging for mapping of regional lung ventilation in patients with COPD. *Radiology*. 2018;286:1040-1051.
- Goralski JL, Chung SH, Glass TM, et al. Dynamic perfluorinated gas MRI reveals abnormal ventilation despite normal FEV1 in cystic fibrosis. *JCI Insight*. 2019;5:e133400.
- Halaweish AF, Moon RE, Foster WM, et al. Perfluoropropane gas as a magnetic resonance lung imaging contrast agent in humans. *Chest*. 2013;144:1300-1310.
- Maunder A, Hughes PJC, Chan H, et al. Comparing 19F C3F8 lung ventilation imaging with hyperpolarized 129Xe: Similarities and limitations. *Proc Intl Soc Mag Reson Med*. 2018;26:1083-1085.
- Miller MR, Hankinson J, Brusasco V, et al. Standardisation of spirometry. *Eur Respir J*. 2005;26:319-338.
- Guyer RA, Hellman MD, Emami K, et al. A robust method for estimating regional pulmonary parameters in presence of noise. *Acad Radiol*. 2008;15:740-752.
- Chon D, Simon BA, Beck KC, et al. Differences in regional wash-in and wash-out time constants for xenon-CT ventilation studies. *Respir Physiol Neurobiol*. 2005;148:65-83.
- Kirby M, Svenningsen S, Owringi A, et al. Hyperpolarized 3He and 129Xe MR imaging in healthy volunteers and patients with chronic obstructive pulmonary disease. *Radiology*. 2012;265:600-610.
- Gutberlet M, Kaireit TF, Voskrebenezv A, et al. Repeatability of regional lung ventilation quantification using fluorinated (19F) gas magnetic resonance imaging. *Acad Radiol*. 2019;26:395-403.
- Wild JM, Ajraoui S, Deppe MH, et al. Synchronous acquisition of hyperpolarised 3He and 1H MR images of the lungs—Maximising mutual anatomical and functional information. *NMR Biomed*. 2011;24:130-134.
- Wild JM, Marshall H, Norquay G, Parnell SR, Clemence M, Griffiths PD. Simultaneous imaging of lung structure and function with triple-nuclear hybrid MR imaging. *Radiology*. 2013;267:251-255.
- Neal MA, Pippard BJ, Hollingsworth KG, et al. Optimized and accelerated 19F-MRI of inhaled perfluoropropane to assess regional pulmonary ventilation. *Magn Reson Med*. 2019;82:1301-1311.
- Obert AJ, Gutberlet M, Kern AL, et al. 1H-guided reconstruction of 19F gas MRI in COPD patients. *Magn Reson Med*. 2020;84:1336-1346.
- He M, Kaushik SS, Robertson SH, et al. Extending semiautomatic ventilation defect analysis for hyperpolarized 129Xe ventilation MRI. *Acad Radiol*. 2014;21:1530-1541.
- Li C, Gore JC, Davatzikos C. Multiplicative intrinsic component optimization (MICO) for MRI bias field estimation and tissue segmentation. *Magn Reson Imaging*. 2014;32:913-923.

**How to cite this article:** McCallister A, Chung SH, Antonacci M, et al. Comparison of single breath hyperpolarized <sup>129</sup>Xe MRI with dynamic <sup>19</sup>F MRI in cystic fibrosis lung disease. *Magn Reson Med*. 2021;85:1028–1038. <https://doi.org/10.1002/mrm.28457>